Performance comparison of different medical image fusion algorithms for clinical glioma grade classification with advanced magnetic resonance imaging (MRI

scientific reports

Check for updates

OPEN

Performance comparison of different medical image fusion algorithms for clinical glioma grade classification with advanced magnetic resonance imaging (MRI)

Amir Khorasani[1], Nasim Dadashi serej[2,3], Milad jalilian[4], Azin Shayganfar[5] & Mohamad Bagher Tavakoli[1]✉

Non-invasive glioma grade classification is an exciting area in neuroimaging. The primary purpose of this study is to investigate the performance of different medical image fusion algorithms for glioma grading purposes by fusing advanced Magnetic Resonance Imaging (MRI) images. Ninety-six subjects underwent an Apparent diffusion coefficient (ADC) map and Susceptibility-weighted imaging (SWI) MRI scan. After preprocessing, the different medical image fusion methods used to fuse ADC maps and SWI were Principal Component Analysis (PCA), Structure-Aware, Discrete Cosine Harmonic Wavelet Transform (DCHWT), Deep-Convolutional Neural network (DNN), Dual-Discriminator conditional generative adversarial network (DDcGAN), and Laplacian Re-Decomposition (LRD). The Entropy, standard deviation (STD), peak signal-to-noise ratio (PSNR), structural similarity index measure (SSIM), and Relative Signal Contrast (RSC) were calculated for qualitative and quantitative analysis. We found high fused image quality with LRD and DDcGAN methods. Further quantitative analysis showed that RSCs in fused images in Low-Grade glioma (LGG) were significantly higher than RSCs in High-Grade glioma (HGG) with PCA, DCHWT, LRD, and DDcGAN. The Receiver Operating Characteristic (ROC) curve test highlighted that LRD and DDcGAN have the highest performance for glioma grade classification. Our work suggests using the DDcGAN and LRD networks for glioma grade classification by fusing ADC maps and SWI images.

Glioma is a brain tumor originating from glial cells in the brain and spinal cord. Every year, almost 100,000 people worldwide are diagnosed with glioma[1]. Glioma is recognized as a serious, worldwide public health concern because of substantial mortality and morbidity[1]. According to the tumor aggressiveness and molecular marker[2], the World Health Organization (WHO) classified glioma grade into Low-Grade glioma (LGG) and High-Grade glioma (HGG)[3]. Glioma grade plays an essential role in managing and treating glioma tumors.

The current clinical method and the gold standard for glioma grade detection are based on histopathological findings from tumor tissue sampling. Despite its long clinical success, tissue sampling has some problems in use, such as invasiveness, time consumption, sampling error, etc.[4–6].

In recent years, there has been an increasing interest in using medical imaging modalities for glioma grade detection as a non-invasive and fast method for glioma grading. Several attempts have been made to use the magnetic resonance imaging (MRI) modality for glioma grading as a non-invasive and fast method. Many studies have been published on the application of different MRI image weights, such as diffusion-weighted imaging (DWI)[6–12], susceptibility-weighted imaging (SWI)[4,13–17], perfusion-weighted imaging (PWI)[18–20], and magnetic resonance spectroscopy (MRS)[21–23] for glioma grade classification. A fundamental problem with much of the

[1]Department of Medical Physics, School of Medicine, Isfahan University of Medical Sciences, Isfahan 81746-73461, Iran. [2]Medical Image and Signal Processing Research Center, School of Advanced Technologies in Medicine, Isfahan University of Medical Sciences, Isfahan, Iran. [3]School of computing and engineering, Univesity of West London, London, UK. [4]Department of Neuroscience and Addiction Studies, School of Advanced Technologies in Medicine, Tehran University of Medical Sciences, Tehran, Iran. [5]Department of Radiology, School of Medicine, Isfahan University of Medical Sciences, Isfahan, Iran. ✉email: mbtavakoli@mui.ac.ir

literature on using single MRI image weights for glioma grading is the low accuracy of these methods. It is well known that combining data from different sources can increase the glioma grade classification accuracy. Several attempts have been made to utilize simple binary logistic regression models to increase the glioma grading accuracy by 'image data' combination[4,24,25]. The main weakness of this method is that they offer no visible and tangible results. Recent developments in image fusion methods have led to introduce algorithms for fusing two different images to create one image that contains the information of the source images, which will be much more helpful for physicians in the clinic.

In recent years, there has been an increasing interest in introducing different image fusion methods, and researchers have proposed different methods such as generative adversarial network (GAN)[26], Laplacian Re-Decomposition (LRD)[27], Principal Component Analysis (PCA)[28], Structure-Aware[29], Discrete Cosine Harmonic Wavelet Transform (DCHWT)[30], Deep-Convolutional Neural network (DNN)[31], Dual-Discriminator conditional generative adversarial network (DDcGAN)[32], etc. Some preliminary works[5,33] were carried out recently to use medical image fusion methods with MRI images for glioma grade classification purposes. It has now been demonstrated that the accuracy of glioma grade classification can be improved with the fusion of different MRI image weights[5,33]. Recently investigators have examined the effect of different MRI image weights fusion on the accuracy of glioma grade classification. They suggest that SWI and ADC map fusion have the highest performance for glioma grade classification[33]. For this reason, we will also use SWI and ADC maps in the present study.

The clinical performance of various fusion methods in relation to glioma grading, particularly when incorporating different MRI image weights, remains a topic that lacks clarity. Therefore, the primary objective of our study was to address this knowledge gap by thoroughly investigating the clinical performance of different image fusion techniques for glioma grade classification. Specifically, we focused on evaluating the effectiveness of fusion methods such as DDcGAN, LRD, PCA, DCHWT, Structure-Aware, and DNN in accurately classifying glioma grades. It is worth noting that, to the best of our knowledge, no previous study has delved into the clinical performance of different medical image fusion methods specifically for glioma grade classification. Consequently, our research takes a pioneering approach in this area. Considering the novelty and importance of this study, we aimed to fuse the SWI and ADC maps of glioma using various fusion methods. This fusion process was carried out to classify LGG and HGG. Subsequently, we meticulously compared these fusion methods' outcomes by employing image quality assessments and quantitative parameters for Glioma grade classification.

Results

Ninety-six patients were recruited for this study according to our inclusion criteria (49 male, 47 female with [36 84] age range). The patients were divided into the HGGs and LGGs based on their histopathological results. Just over half the samples (59.3%) were HGGs. No significant differences were found in sex and age between HGGs and LGGs.

Figures 1 and 2 show the results obtained from the different fusion methods. Figures 1 and 2 provide the fused ADC map and SWI image of an HGG and LGG patient, respectively, among the six fusion methods.

Table 1 and Fig. 3 show the results of comparative analysis and image quality parameters of the fused image with different fusion methods. As shown in Table 1 and Fig. 3, the results indicate that the fused images with LRD and DDcGAN significantly have the highest image quality compared with other fused methods. The average STD

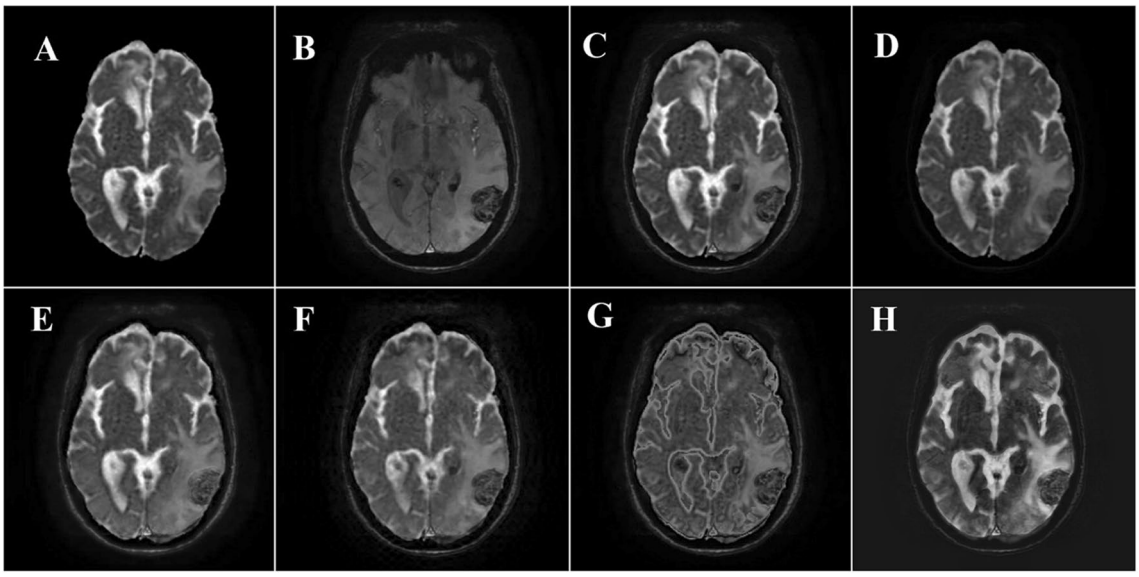

Figure 1. Source images and the result of different fusion methods of a 67-man with HGG. (**A**) ADC map. (**B**) SWI image. (**C**) Fused image with Structure-Aware method. (**D**) Fused image with PCA method. (**E**) Fused image with LRD method. (**F**) Fused image with DCHWT method. (**G**) Fused image with DNN method. (**H**) Fused image with DDcGAN method.

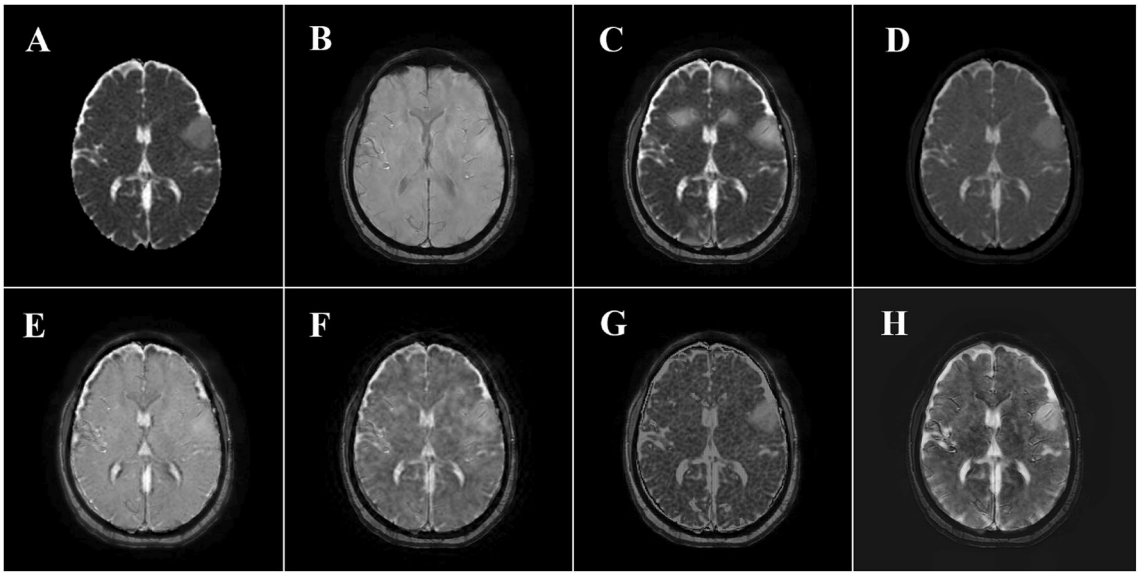

Figure 2. Source images and the result of different fusion methods of a 58 woman with LGG. (**A**) ADC map. (**B**) SWI image. (**C**) Fused image with Structure-Aware method. (**D**) Fused image with PCA method. (**E**) Fused image with LRD method. (**F**) Fused image with DCHWT method. (**G**) Fused image with DNN method. (**H**) Fused image with DDcGAN method.

Fusion method	Entropy	STD	PSNR	SSIM	Runtime (s)
PCA	6.321	46.23	36.565	0.592	0.064
Structure-Aware	6.279	46.38	31.820	0.571	1.162
DCHWT	6.421	48.06	30.670	0.593	4.075
LRD	6.921	**62.48**	46.620	0.652	982.12
DNN	5.621	38.34	32.960	0.267	0.95
DDcGAN	**7.140**	59.19	**46.780**	**0.695**	1.27

Table 1. Average of Entropy, STD, PSNR, and SSIM of fused ADC map and SWI MRI image weights with different fusion methods. Highest values are in bold.

and entropy of the original ADC maps were calculated to be 47.02 and 5.094, respectively. For the SWI images, these values were 45.16 and 5.968, respectively.

To evaluate the clinical performance of different fusion methods, the average RSC of fused ADC map and SWI of LGGs and HGGs were compared in different fusion methods. From the data in Fig. 4, there were no significant differences in RSCs of fused images between LGGs and HGGs with Structure-Aware and DNN fusion methods. Further analysis showed that RSCs in LGGs are significantly higher than RSCs in HGGs in fused images with PCA, DCHWT, LRD, and DDcGAN fusion methods.

ROC analysis was used to analyze the performance of different fusion methods for glioma grade quantitative classification on fused ADC maps and SWI images. Table 2 and Fig. 5 present the summary ROC analysis for glioma grade classification in ADC map and SWI fused images with different fusion methods. Interestingly, the LRD and DDcGAN have the highest performance for glioma grade classification on fused ADC maps and SWI images.

Discussion

As mentioned in the literature review, glioma grade classification with different MRI images are very interesting. Prior studies that have noted the importance of data combination used simple logistic regression of MRI image data to increase the glioma grade classification accuracy[4,24,25]. A large number of image fusion methods have been reported in the literature. On the other hand, although the development of medical image fusion is exciting and popular, its clinical application for glioma grade classification has received little attention. This study assessed the importance of different image fusion methods in clinical glioma grade classification and image quality. The present study was designed to determine the clinical performance of different medical image fusion methods such as PCA, Structure-Aware, DCHWT, DNN, DDcGAN, and LRD for glioma grading with fusing ADC maps and SWI images.

The current study compared the quality of fused images with Entropy, STD, PSNR, and SSIM factors as the performance metrics. Interestingly, comparisons on image quality metrics demonstrated that the DDcGAN and

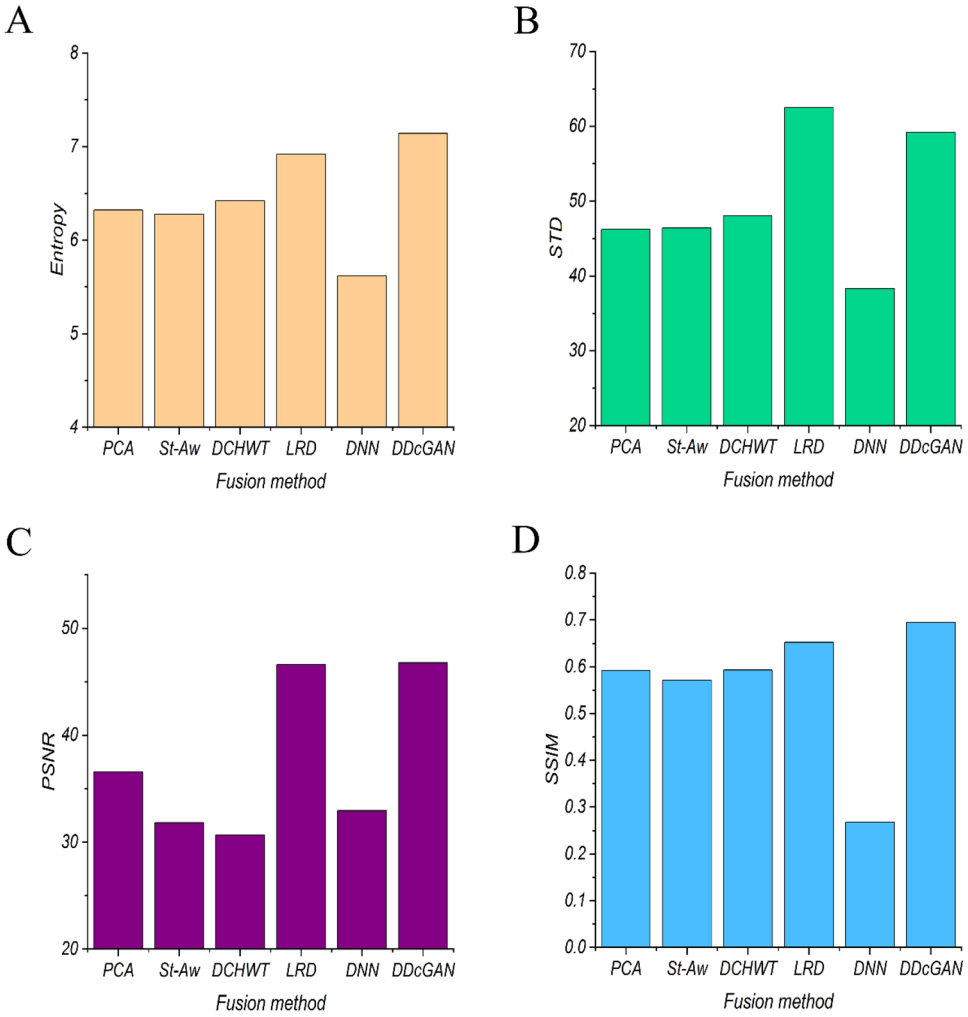

Figure 3. Comparative analysis of different fusion methods with image quality parameters (**A**) average Entropy, (**B**) average STD, (**C**) average PSNR, and (**D**) average SSIM in different fusion methods for fusing ADC maps and SWI images.

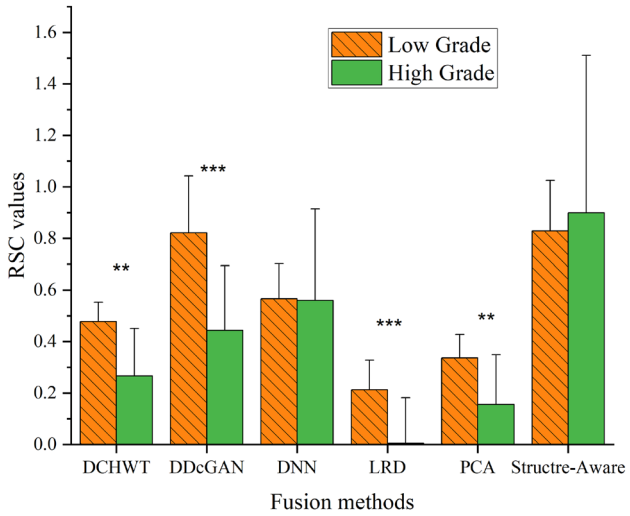

Figure 4. Average RSCs in LGGs and HGGs in fused ADC maps and SWI images in different fusion methods. Values are in Average ± standard deviation. ** *P* Value < 0.05, *** *P* Value < 0.01.

Fusion method	Cut-off Value	AUC	Sensitivity	Specificity
PCA	0.1151	0.827	0.818	0.720
DCHWT	0.4087	0.882	0.909	0.812
LRD	0.1923	**0.945**	**0.916**	**0.843**
DDcGAN	0.6197	**0.956**	**0.975**	**0.918**

Table 2. Parameters of ROC curve analysis for quantitative glioma grade classification on fused ADC map and SWI images with different fusion methods. Highest values are in bold.

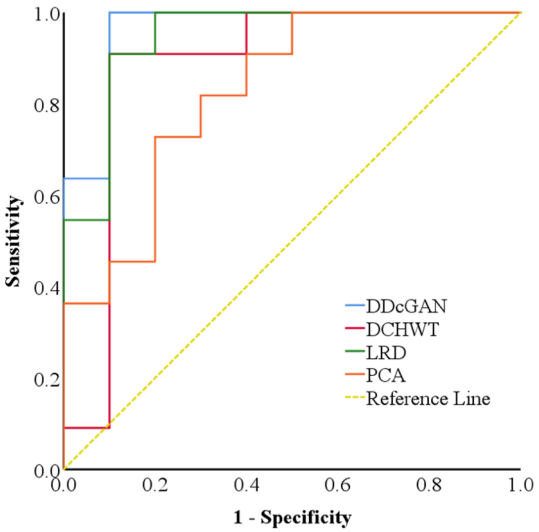

Figure 5. ROC curve of different fusion methods for glioma grade classification on fused ADC maps and SWI images.

LRD algorithms identify the most valuable image data and keep approximately the most considerable amount of information from the source images in the fused image. These results match those observed in earlier studies. As proposed by[32] and[27], the evidence we found points to the high performance of the DDcGAN and LRD fusion method compared with other methods. Although DDcGAN and LRD have the same performance for ADC map and SWI image fusion, the average runtime of DDcGAN on the testing image pairs is significantly lower than LRD runtime. Therefore, it seems that we can use DDcGAN for the ADC map and SWI image fusion with adequate fused image quality. What is surprising is that, DNN has the lowest fused image quality and performance for ADC map and SWI image fusion. A possible explanation for these results may be our limited image data set for DNN training. Further work is required to train DNN with much more image.

The quantitative analysis did not show any RSCs significant difference in the fused image with DNN and Structure-Aware algorithm between LGGs and HGGs. Fused images with PCA, DCHWT, LRD, and DDcGAN algorithms provided the significant RSCs difference between LGGs and HGGs. There is a consensus among studies that used ADC maps and SWI images for glioma grade classification[4,9–13,16,17,23]. Interestingly, in fused images, RSCs in LGGs are significantly higher than HGGs with PCA, DCHWT, LRD, and DDcGAN algorithms. These values correlate satisfactorily with previous studies and further support the role of tumor cellularity and micro bleeding in HGGs[4,5,33]. In accordance with the present results, previous studies have demonstrated that tumor cellularity increased with glioma grade, and HGGs have lower ADC values in DWI images than LGGs[34–36]. The findings observed in SWI images mirror those of the previous studies that have examined the SWI image performance for glioma grading[13,37]. The findings of previous studies showed, in HGGs, average pixel intensities of SWI images were lower than LGGs.

The most remarkable result from ROC analysis is that the DDcGAN and LRD fusion algorithms achieve the best performance in the glioma grade classification with ADC map and SWI fusion. It seems possible that these results are due to the advantage of GAN networks in feature extraction in the DDcGAN algorithm and well retain image structure data and fully considering the redundant and complementary data between high-frequency sub-band images in the LRD algorithm. These findings suggest that image fusion of ADC map and SWI with DDcGAN and LRD networks can be used for glioma grade classification in the clinic.

This investigation aimed to determine the clinical performance of PCA, Structure-Aware, DCHWT, DNN, DDcGAN, and LRD image fusion algorithms for glioma grade classification by fusing ADC maps and SWI images. Results indicated that the DDcGAN and LRD showed superiority over PCA, Structure-Aware, DCHWT, and DNN for glioma grade classification not only in qualitative analysis and fused image quality but also in

quantitative analysis. However, the long-running time of the LRD algorithm cannot be ignored. For the first time, this study has demonstrated that we can use the DDcGAN network for glioma grade classification with high image quality and performance by fusing ADC maps and SWI images. The major limitation of this study is based on the small sample size. The current code runtime was limited by computer hardware. As you know, the duration of neural network training is inversely dependent on GPU processing power. It is recommended that future research be undertaken with powerful GPUs, CPUs, and a bigger sample size. Further research on optimizing and speeding up the LRD medical image fusion would be interesting. More research is required to determine the efficacy of different medical image fusion methods in the clinic, especially in radiation therapy for fusing MRI and computed tomography (CT) images for treatment planning. It would be interesting to assess the effectiveness of LRD and DDcGAN networks in radiation therapy treatment planning systems.

Material and methods

Patient

Criteria for patient selection were as follow:

1- Histopathology confirmation of the glioma.
2- No radiotherapy or chemotherapy was performed before the MRI exam.
3- High image quality without any MRI artifacts.
4- No claustrophobia to the MRI.
5- Do not have an allergy to the gadolinium-based contrast agent.
6- Do not have a pregnancy.

Before the head MRI scan, all participants provided informed consent, and the Isfahan University of medical sciences, Isfahan, Iran, research ethics committee approved the study with ID: IR.MUI.RESEARCH.REC.1400.237 and all parts of the experiment were performed in accordance with relevant guidelines and regulations.

Imaging

All patients were scanned by a clinical 1.5T MR scanner (GE MRI signal explorer 1.5T) with conventional T_1, T_2, T_2-FLAIR, T_1 enhancement, DWI-weighted (ADC map), and SWI pulse sequences. The parameters of the pulse sequences are listed in Table 3.

Preprocessing

Noise reduction and image smoothing, normalization, and registration techniques were used to enhance image quality and processing capability. Denoising, normalizing, image smoothing, and registration were performed using homemade custom code written in Python programming language.

Noise reduction

The noise reduction and image smoothing processes increased input image quality for medical image analysis. Noise reduction was employed since this is an essential preprocessing step in medical image analysis. This study used the Deep-Learning based model, a Convolutional autoencoder network, for image denoising purposes. Our convolutional autoencoder network for denoising proceeds in the same way as indicated in[38]. The encoding part consists of two convolutional layers and two max-pooling layers. The decoding consists of two convolutional layers and two upsampling layers, and in the last layer, we used a convolutional layer with one filter. More details are given in the original paper[38].

Normalization

Ideally, image pixel values and contrast represent the imaged tissue properties. Nevertheless, image pixel values change due to noise and imaging artifacts. Normalization aims to reduce the effect of noise and imaging artifacts on the image's pixel values. We used the Removal of Artificial Voxel Effect by Linear Regression (RAVEL) method to do the normalization process. The RAVEL method is essentially the same as that used by Fortin et al.[39].

Image registration

Image registration was done to align source images into one framework. So corresponding pixels of each source image show similar tissue points of the patient body. The Landmark-Based registration method is used to register source images[40]. This method was chosen because it is one of the most practical and straightforward ways to image registration[40]. An experienced team of neuroimaging experts and radiologists manually annotated anatomical landmarks in each MRI image, including Anterior and Posterior Commissures (AC-PC), corpus

Image weights	TR (ms)	TE (ms)	FOV (mm)	b-value (s/mm^2)	Matrix size	Thickness (mm)	Gap (mm)
ADC	5211	110	240 × 240	50–1000	256 × 256	5	5
SWI	87	47.5	240 × 240	–	256 × 256	5	5

Table 3. Parameters of Magnetic resonance imaging (MRI) pulse sequences. TR; time of repetition. TE; time of echo. FOV; field of view.

callosum, interhemispheric fissure, offer valuable landmarks, Ventricles, Basal Ganglia, Cerebellum, etc. based on Glioma location. A non-rigid transformation model using B-splines was selected for the alignment and transformation stage based on the detected landmarks and their correspondence[41–43]. The transformation parameters were estimated using a registration optimization algorithm to minimize the differences between corresponding landmarks and achieve accurate alignment[44]. The source image was then resampled and transformed using the B-spline interpolation[41,42] techniques to map each voxel to its new position in the target image domain. Thus, the images are registered and ready for fusion.

Fusion

The current study uses various medical image fusion methods to compare the glioma grading performance of these methods with the Dual-Discriminator conditional generative adversarial network (DDcGAN)[32] and Laplacian Re-Decomposition (LRD)[27] methods. This method included Principal Component Analysis (PCA), Structure-Aware, Discrete Cosine Harmonic Wavelet Transform (DCHWT), Deep-Convolutional Neural Network (DNN), DDcGAN, and LRD.

Dual-Discriminator conditional generative adversarial network (DDcGAN)

For this study, the DDcGAN was used to fuse SWI and ADC maps for glioma grading purposes. The overall DDcGAN architecture is shown in Fig. 6. DDcGAN was created according to the procedure proposed by Ma et al.[32]. The DDcGAN goal is to learn a generator to generate fused image F to be informative and realistic enough to fool the discriminators.

The generator architecture is presented in Fig. 7 and consists of two deconvolution layers, an encoder section, and a decoder section. Deconvolution layers obtain the feature map of the source images. These feature maps are concatenated and used as an input image of the encoder network.

The encoder network consists of five convolutional layers. Each convolutional layer consists of a 3×3 filter size with stride 1, batch normalization, and ReLU activation function. Short direct connection and DenseNet[45] are used between each layer and all layers in a feed-forward fashion. The fused feature maps are produced as the output of the encoder network. Following this, the encoder output is fed to the decoder network to generate and reconstruct fused images.

The decoder part is also made of five convolutional layers, as shown in Fig. 7. The decoder layers are very similar to the encoder layers, except that tanh is used as the activation function of the last layer of the decoder part.

The design of DDcGAN architecture was based on the use of two discriminators. The architecture of the discriminators D_1 and D_2 are similar, as shown in Fig. 8. D_1 and D_2 are made of three convolutional and one fully connected layer. Convolutional layers consist of a 3×3 filter size with different filter numbers, batch normalization, and ReLU activation function. In the fully connected layer, the tanh activation function was used. The DDcGAN architecture we used is detailed in[32].

Laplacian re-decomposition (LRD)

The several steps of LRD fusion methods are in Fig. 9. Briefly, In the LRD methods, each source image's enhancement images (HA and HB) are produced by Gradient Domain Image Enhancement (GDIE). Following this, by using Laplacian pyramid transform (LP) from H_A and H_B images, High-frequency (L_A and L_B) and Low-frequency (G_A and G_B) sub-band images were created. The Overlapping domain (O_A and O_B) and non-overlapping domain (N_A and N_B) images were created with the Decision Graph Re-decomposition (DGR). In the last stage of the LRD fusion method, with different fusion rules such as local energy maximum (LEM), overlapping domain (OD), non-overlapping domain (NOD), inverse re-decomposition scheme (IRS), and inversed LP, the fused image was reconstructed. More details of this medical fusion algorithm are in[27]. We used the MATLAB software package for writing and running LRD fusion code.

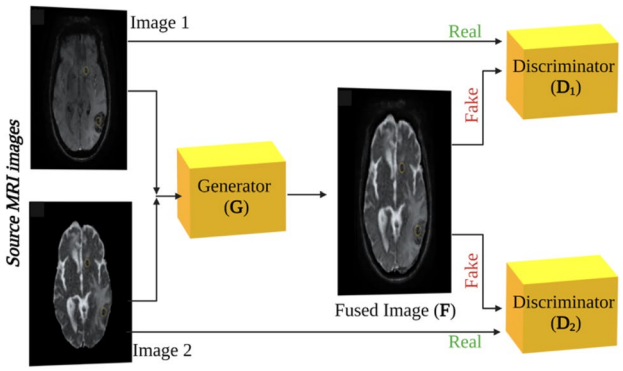

Figure 6. the overall DDcGAN for SWI and ADC map MRI image fusion for glioma grading.

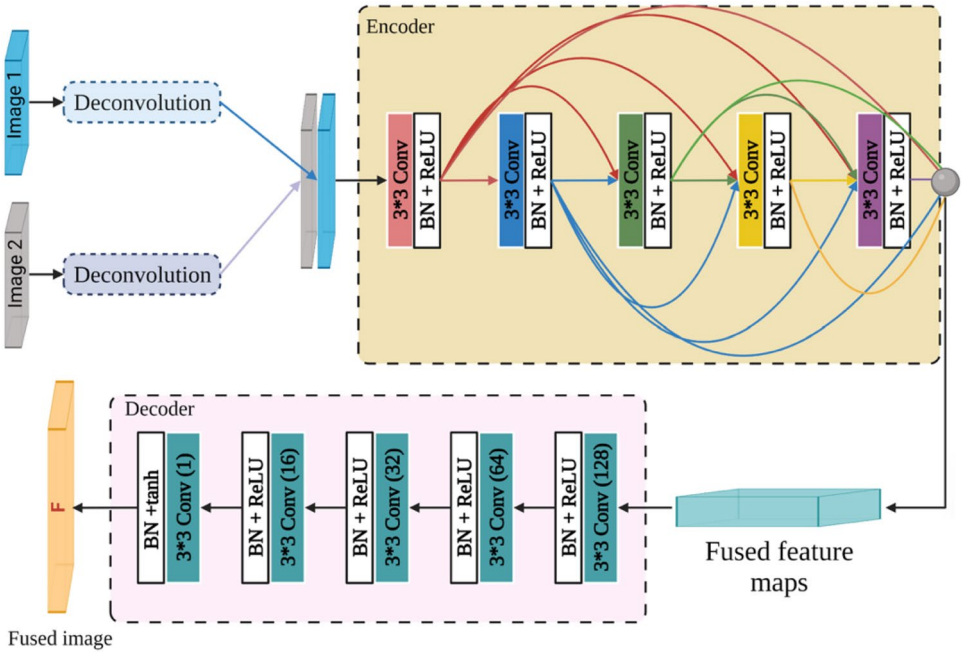

Figure 7. the generator architecture, including encoder and decoder networks. 3*3 is the filter size, Conv (n) is the convolution layer with n filter number, BN is batch normalization, and ReLU and tanh are activation functions.

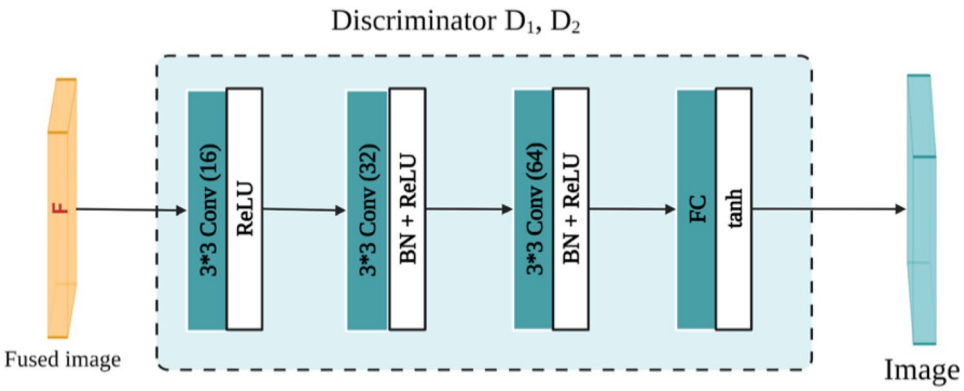

Figure 8. the Discriminator architecture. 3 × 3 is the filter size, Conv (n) is the convolution layer with n filter number, BN is batch normalization, ReLU and tanh are activation functions, and FC is fully connected.

PCA, Structure-Aware, DCHWT, and DNN medical image fusion methods

In fact, to compare the DDcGAN and LRD performance for glioma grading, we used different image fusion methods such as PCA, Structure-Aware, DCHWT, and DNN. For example, the general structure of the DNN is shown in Fig. 10. In this section, our goal is not to describe the details of each fusion method. Details can be found in the original paper on the proposed fusion methods[27–32].

Performance analysis of fusion methods

Most recent studies have measured fused image visual quality in different accepted standard ways[46]. These standard factors are Entropy, standard deviation (STD), peak signal-to-noise ratio (PSNR), and structural similarity index measure (SSIM)[46].

Entropy

Image entropy is a metric used to quantify the amount of information or randomness present in an image. It measures the average uncertainty or disorder within the image. In other words, image entropy provides a measure of the complexity or variability of pixel values in an image. Entropy is calculated based on the probability distribution of pixel intensities within the image. A higher entropy value indicates more significant variability

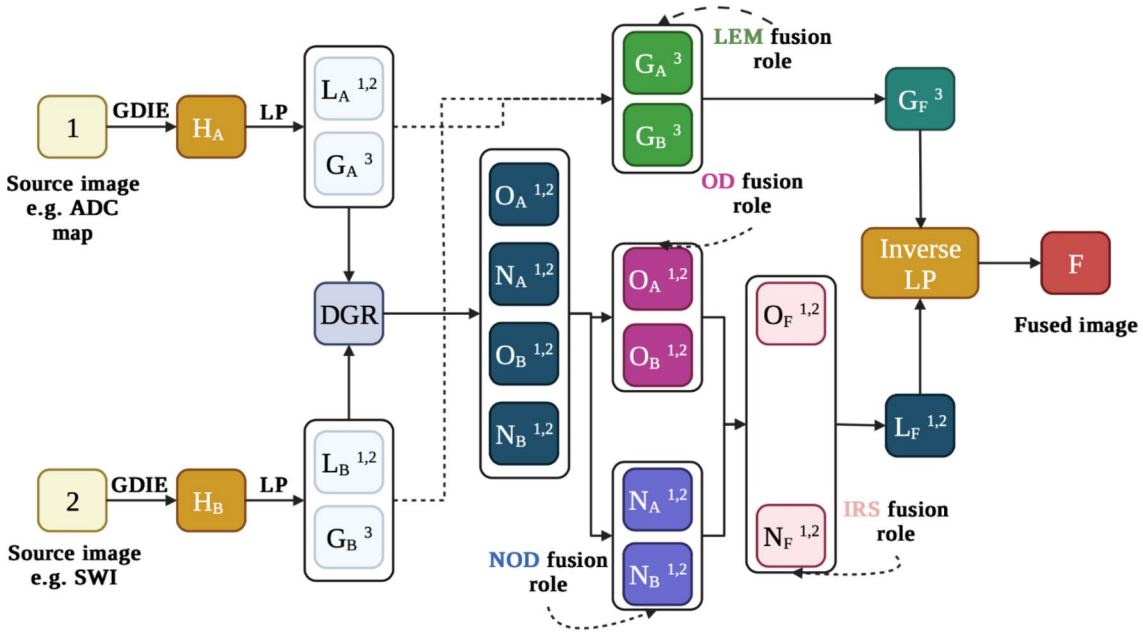

Figure 9. The overall LRD fusion method for medical image fusion. In this algorithm, 1 and 2: source images, H_A and H_B: enhancement images, L_A and L_B: High-frequency sub-band images, G_A and G_B: Low-frequency sub-band images, O_A and O_B: overlapping domain images, N_A and N_B: Non-overlapping domain images, O_F: overlapping domain fusion images, N_F: Non-overlapping domain fusion images, G_F: low-frequency sub-band fusion images, L_F: high-frequency sub-band fusion images, F: fused image.

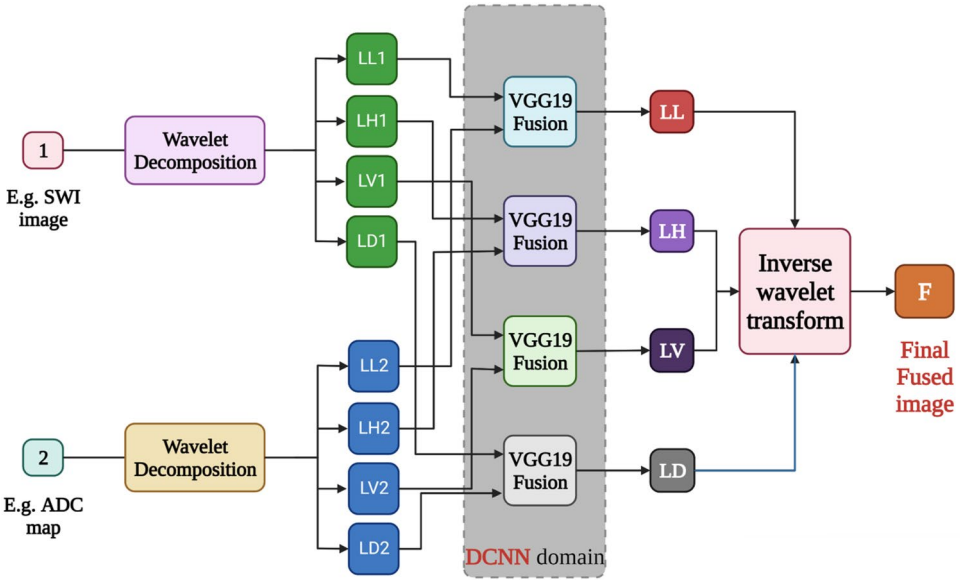

Figure 10. The overall DNN fusion method for medical image fusion.

and randomness in the pixel values, while a lower entropy value suggests a more uniform or predictable distribution. Entropy is calculated as follows[46]:

$$entropy = -\sum_{L=0}^{L-1} P_i \times \log_2 P_i \tag{1}$$

where L is the gray level number in the image, P is the probability density function for the gray level of *i*. The range of image entropy depends on the number of intensity levels used for quantization. If an image is represented using 'L' discrete intensity levels (e.g., 8-bit grayscale images with 256 levels), then the entropy values typically range from 0 to log2(L). In an 8-bit grayscale image (L = 256), the entropy values can range from 0 to 8. Entropy is proportional to the amount of fused image information in fused images.

STD

Image STD is a statistical measure that quantifies the amount of variation or dispersion in pixel intensities within an image. It provides information about the spread of pixel values around the mean intensity. STD is used to measure the image contrast of the fused image. The higher STD values represent more helpful information and high contrast of the fused image. STD calculated as[46]:

$$STD = \sqrt{\frac{\sum_{i=1}^{M}\sum_{j=1}^{N}\left(f(i,j)-\mu\right)^2}{M \times N}} \tag{2}$$

where M and N are the length and width of the fused image, f(i,j), μ is the average gray value of the fused image.

PSNR

PSNR is a quantitative value based on mean square error. The higher PSNR value in the fused image is better and calculated as follows[46]:

$$PSNR = 10 \times \log_{10}\left(\frac{L^2}{RMSE^2}\right) \tag{3}$$

where L is the maximum gray level value in the fused image, and RMSE is the mean square error and calculated with the following equation[46]:

$$RMSE = \sqrt{\frac{\sum_{m=1}^{M}\sum_{n=1}^{N}[A(m,n)-F(m,n)]^2}{M \times N}} \tag{4}$$

A(m, n) and F(m, n) represent the intensity value of the source and fused images, respectively. M and N are the length and width of images.

SSIM

SSIM is a factor that measures the structural similarity between the source image and the fused image. SSIM values between 0 and 1 and higher SSIM values indicate a higher structural similarity between the two images. SSIM calculated as[46]:

$$SSIM_{(A,B,F)} = \frac{SSIM_{(A,F)} + SSIM_{(B,F)}}{2} \tag{5}$$

$$SSIM_{(A,F)} = \frac{(2\mu_A\mu_F + C_1)(2\sigma_{AF} + C_2)}{\left(\mu_A^2 + \mu_F^2 + C_1\right)\left(\sigma_A^2 + \sigma_F^2 + C_2\right)} \tag{6}$$

$$SSIM_{(B,F)} = \frac{(2\mu_B\mu_F + C_1)(2\sigma_{BF} + C_2)}{\left(\mu_B^2 + \mu_F^2 + C_1\right)\left(\sigma_B^2 + \sigma_F^2 + C_2\right)} \tag{7}$$

A and B are source images, and F is the fused image. In these equations, μ is the average value, and σ is the variance of source and fused images. C_1 and C_2 are small constants added for numerical stability.

Quantitative evaluation

The study uses quantitative analysis to gain insights into the clinical application of different fusion methods for glioma grading with MRI images. For the quantitative analysis, for each patient, the image slice with the largest tumor size and the highest quality was selected for data evaluation by two radiologists. To determine the Relative Signal Contrast (RSC) values, the mean signal intensity of circular regions of interest (ROI) in each image was calculated. Radiologists manually drew the ROIs with ImageJ software packages. Three ROIs were sampled and averaged for each region to improve the comparison's power. Then, RSC was calculated by the following equation[5,33]:

$$RSC_{ROI} = \frac{\mu_{ROI} - \mu_{WM}}{\mu_{WM}} \tag{8}$$

μ_{ROI} Is the mean signal intensity of the active tumor region, and μ_{WM} Is the mean signal intensity of the white matter in each picture. RSCs in fused images of LGGs and HGGs with different fusion methods were calculated and compared with each other for glioma grading performance.

Statistical analysis

Data management and analysis were performed using SPSS 26.0 software (IBM Corp. Armonk, NY, USA). Kolmogorov–Smirnov test can be used to assess the normality distribution of the data. We could compare RSCs between LGGs and HGGs using the two-tailed unpaired student's T-Test. We used the Exact Fisher test to evaluate the sex and age relationship with the glioma grade. The *P* values of less than 0.05 were indicated to be statistically significant. The significant RSCs for the LGGs and HGGs were subjected to receiver operating characteristic (ROC) curve analysis to determine the cut-off values, the area under the curve (AUC), sensitivity,

and specificity for glioma grade classification in fused MRI images with different fusion methods. The area under the curve (AUC) was calculated with the cut-off value set as the maximum Youden index.

Data availability

The datasets used and analyzed during the current study are available from the corresponding author upon reasonable request.

Received: 9 May 2023; Accepted: 29 September 2023
Published online: 17 October 2023

References

1. Molinaro, A. M., Taylor, J. W., Wiencke, J. K. & Wrensch, M. R. Genetic and molecular epidemiology of adult diffuse glioma. *Nat. Rev. Neurol.* **15**(7), 405–417 (2019).
2. Mesfin, F. B. & Al-Dhahir, M. A. "Gliomas," (2017).
3. Louis, D. N. *et al.* The 2021 WHO classification of tumors of the central nervous system: A summary. *Neuro. Oncol.* **23**(8), 1231–1251 (2021).
4. Khorasani, A. & Tavakoli, M. B. Multiparametric study for glioma grading with FLAIR, ADC map, eADC map, T1 map, and SWI images. *Magn. Reson. Imaging* **96**, 93–101 (2023).
5. Khorasani, A., Tavakoli, M. B., Saboori, M. & Jalilian, M. Preliminary study of multiple b-value diffusion-weighted images and T1 post enhancement magnetic resonance imaging images fusion with Laplacian Re-decomposition (LRD) medical fusion algorithm for glioma grading. *Eur. J. Radiol. Open* **8**, 100378 (2021).
6. Hakyemez, B. *et al.* High-grade and low-grade gliomas: Differentiation by using perfusion MR imaging. *Clin. Radiol.* **60**(4), 493–502 (2005).
7. Ryu, Y. J. *et al.* Glioma: application of whole-tumor texture analysis of diffusion-weighted imaging for the evaluation of tumor heterogeneity. *PLoS One* **9**(9), e108335 (2014).
8. Kang, Y. *et al.* Gliomas: Histogram analysis of apparent diffusion coefficient maps with standard-or high-b-value diffusion-weighted MR imaging—correlation with tumor grade. *Radiology* **261**(3), 882–890 (2011).
9. Suh, C. H., Kim, H. S., Jung, S. C. & Kim, S. J. Diffusion-weighted imaging and diffusion tensor imaging for differentiating high-grade glioma from solitary brain metastasis: A systematic review and meta-analysis. *Am. J. Neuroradiol.* **39**(7), 1208–1214 (2018).
10. Gihr, G. A. *et al.* Histogram analysis of diffusion weighted imaging in low-grade gliomas: In vivo characterization of tumor architecture and corresponding neuropathology. *Front. Oncol.* **10**, 206 (2020).
11. Al-Agha, M., Abushab, K., Quffa, K., Al-Agha, S., Alajerami, Y., Tabash, M. "Efficiency of high and standard b value diffusion-weighted magnetic resonance imaging in grading of gliomas," *J. Oncol.*, vol. **2020**, (2020)
12. Kusunoki, M. *et al.* Differentiation of high-grade from low-grade diffuse gliomas using diffusion-weighted imaging: A comparative study of mono-, bi-, and stretched-exponential diffusion models. *Neuroradiology* **62**(7), 815–823 (2020).
13. Hsu, C. C., Watkins, T. W., Kwan, G. N. C. & Haacke, E. M. Susceptibility-weighted imaging of glioma: Update on current imaging status and future directions. *J. Neuroimaging* **26**(4), 383–390 (2016).
14. Di Ieva, A. *et al.* Three-dimensional susceptibility-weighted imaging at 7 T using fractal-based quantitative analysis to grade gliomas. *Neuroradiology* **55**(1), 35–40 (2013).
15. Su, C.-Q., Lu, S.-S., Han, Q.-Y., Zhou, M.-D. & Hong, X.-N. Intergrating conventional MRI, texture analysis of dynamic contrast-enhanced MRI, and susceptibility weighted imaging for glioma grading. *Acta radiol.* **60**(6), 777–787 (2019).
16. Chuang, T.-C. *et al.* Intra-tumoral susceptibility signal: A post-processing technique for objective grading of astrocytoma with susceptibility-weighted imaging. *Quant. Imaging Med. Surg.* **12**(1), 558 (2022).
17. Hassan, A. A. A., Abdel-Aziz, A. M. R., Aziz, T. T. A., Twadros, S. R. & Mamdouh, F. Role of susceptibility weighted images (SWI) in grading of brain glioma. *QJM An Int. J. Med.* **114**, 106–017 (2021).
18. Alkanhal, H., Das, K. & Poptani, H. Diffusion-and perfusion-weighted magnetic resonance imaging methods in nonenhancing gliomas. *World Neurosurg.* **141**, 123–130 (2020).
19. Seo, M. *et al.* Volumetric measurement of relative CBV Using T1-perfusion-weighted mri with high temporal resolution compared with traditional T2*-perfusion-weighted mri in postoperative patients with high-grade gliomas. *Am. J. Neuroradiol.* **43**(6), 864–871 (2022).
20. Hartmann, M. *et al.* Distinguishing of primary cerebral lymphoma from high-grade glioma with perfusion-weighted magnetic resonance imaging. *Neurosci. Lett.* **338**(2), 119–122 (2003).
21. Toyooka, M. *et al.* Tissue characterization of glioma by proton magnetic resonance spectroscopy and perfusion-weighted magnetic resonance imaging: Glioma grading and histological correlation. *Clin. Imaging* **32**(4), 251–258 (2008).
22. Galijasevic, M. *et al.* Magnetic resonance spectroscopy in diagnosis and follow-up of gliomas: State-of-the-Art. *Cancers (Basel)* **14**(13), 3197 (2022).
23. Yao, R. *et al.* The diagnostic value of apparent diffusion coefficient and proton magnetic resonance spectroscopy in the grading of pediatric gliomas. *J. Comput. Assist. Tomogr.* **45**(2), 269 (2021).
24. Park, S. M., Kim, H. S., Jahng, G. H., Ryu, C. W. & Kim, S. Y. Combination of high-resolution susceptibility-weighted imaging and the apparent diffusion coefficient: added value to brain tumour imaging and clinical feasibility of non-contrast MRI at 3 T. *Br. J. Radiol.* **83**(990), 466–475 (2010).
25. Kim, H. S. & Kim, S. Y. A prospective study on the added value of pulsed arterial spin-labeling and apparent diffusion coefficients in the grading of gliomas. *Am. J. Neuroradiol.* **28**(9), 1693–1699 (2007).
26. Ma, J. *et al.* Pan-GAN: An unsupervised pan-sharpening method for remote sensing image fusion. *Inf. Fusion* **62**, 110–120 (2020).
27. Li, X. *et al.* Laplacian redecomposition for multimodal medical image fusion. *IEEE Trans. Instrum. Meas.* **69**(9), 6880–6890 (2020).
28. Metwalli, M. R., Nasr, A. H., Allah, O. S. F. & El-Rabaie, S. Image fusion based on principal component analysis and high-pass filter. *International Conference on Computer Engineering & Systems* **2009**, 63–70 (2009).
29. Li, W., Xie, Y., Zhou, H., Han, Y. & Zhan, K. Structure-aware image fusion. *Optik (Stuttg)* **172**, 1–11 (2018).
30. Shreyamsha Kumar, B. K. Multifocus and multispectral image fusion based on pixel significance using discrete cosine harmonic wavelet transform. *Signal, Image Video Process.* **7**, 1125–1143 (2013).
31. Hou, R., Zhou, D., Nie, R., Liu, D. & Ruan, X. Brain CT and MRI medical image fusion using convolutional neural networks and a dual-channel spiking cortical model. *Med. Biol. Eng. Comput.* **57**(4), 887–900 (2019).
32. Ma, J., Xu, H., Jiang, J., Mei, X. & Zhang, X.-P. DDcGAN: A dual-discriminator conditional generative adversarial network for multi-resolution image fusion. *IEEE Trans. Image Process.* **29**, 4980–4995 (2020).
33. Khorasani, A., Tavakoli, M. B. & Saboori, M. Using of Laplacian Re-decomposition image fusion algorithm for glioma grading with SWI, ADC, and FLAIR images. *Polish J. Med. Phys. Eng.* **27**(4), 261–269 (2021).
34. Sugahara, T. *et al.* Usefulness of diffusion-weighted MRI with echo-planar technique in the evaluation of cellularity in gliomas. *J. Magn. Reson. Imaging An. Off. J. Int. Soc. Magn. Reson. Med.* **9**, 53–60 (1999).

35. Gauvain, K. M. *et al.* Evaluating pediatric brain tumor cellularity with diffusion-tensor imaging. *Am. J. Roentgenol.* **177**(2), 449–454 (2001).
36. El-Serougy, L., Abdel Razek, A. A. K., Ezzat, A., Eldawoody, H. & El-Morsy, A. Assessment of diffusion tensor imaging metrics in differentiating low-grade from high-grade gliomas. *Neuroradiol. J.* **29**, 400–407 (2016).
37. Lai, P.-H. *et al.* Susceptibility-weighted imaging provides complementary value to diffusion-weighted imaging in the differentiation between pyogenic brain abscesses, necrotic glioblastomas, and necrotic metastatic brain tumors. *Eur. J. Radiol.* **117**, 56–61 (2019).
38. Gondara, L. "Medical image denoising using convolutional denoising autoencoders," in *2016 IEEE 16th international conference on data mining workshops (ICDMW)*, pp. 241–246 (2016).
39. Fortin, J.-P. *et al.* Removing inter-subject technical variability in magnetic resonance imaging studies. *Neuroimage* **132**, 198–212 (2016).
40. Johnson, H. J. & Christensen, G. E. Consistent landmark and intensity-based image registration. *IEEE Trans. Med. Imaging* **21**(5), 450–461 (2002).
41. Ji, H. *et al.* A non-rigid image registration method based on multi-level B-spline and L2-regularization. *Signal, Image Video Process.* **12**(6), 1217–1225. https://doi.org/10.1007/s11760-018-1274-0 (2018).
42. Du, X., Dang, J., Wang, Y., Wang, S. & Lei, T. "A parallel nonrigid registration algorithm based on B-spline for medical images," *Comput. Math. Methods Med.*, vol. **2016**, (2016).
43. Chang, Q., Lu, C. & Li, M. Cascading affine and B-spline registration method for large deformation registration of lung X-rays. *J. Digit. Imaging* **36**(3), 1262–1278. https://doi.org/10.1007/s10278-022-00763-z (2023).
44. Castillo, R. *et al.* A framework for evaluation of deformable image registration spatial accuracy using large landmark point sets. *Phys. Med. Biol.* **54**(7), 1849 (2009).
45. Huang, G., Liu, Z., Van Der Maaten, L. & Weinberger, K. Q. "Densely connected convolutional networks," in *Proceedings of the IEEE conference on computer vision and pattern recognition*, pp. 4700–4708 (2017).
46. Huang, B., Yang, F., Yin, M., Mo, X. & Zhong, C. "A review of multimodal medical image fusion techniques," *Comput. Math. Methods Med.*, vol. **2020**, (2020).

Acknowledgements

The authors thank Isfahan University of Medical Sciences for the financial support of this work.

Author contributions

Conceptualization, A.K., M-B.T.; Methodology, A.K., M.J., A.S.; Validation, A.K., M-B.T.; Investigation, A.K.; Resources, A.K., M-B.T.; Data Curation, A.K., N.D., A.S.; Writing—Original Draft Preparation, A.K.; Writing—Review and Editing, A.K., M-B.T., N.D., M.J., A.S.; Supervision, M-B.T.; Project Administration, A.K., M-B.T.; Funding Acquisition, M-B.T., All authors have read and agreed to the published version of the manuscript.

Funding

This study was supported by Isfahan University of Medical Sciences, Isfahan, I.R. Iran (grant number 240088).

Competing interests

The authors declare no competing interests.

Additional information

Correspondence and requests for materials should be addressed to M.B.T.

Reprints and permissions information is available at www.nature.com/reprints.

Publisher's note Springer Nature remains neutral with regard to jurisdictional claims in published maps and institutional affiliations.